

# A pilot study of interplanetary scintillation with FAST

Li-Jia Liu,<sup>1,2</sup> Bo Peng,<sup>1\*</sup> Lei Yu,<sup>1,2\*</sup> Ye-Zhao Yu,<sup>3</sup> Ji-Guang Lu,<sup>1</sup> Bin Liu,<sup>1\*</sup> O. Chang<sup>1b,4</sup>, M. M. Bisi<sup>4</sup>  
and the FAST Collaboration<sup>1</sup>

<sup>1</sup>CAS Key Laboratory of FAST, National Astronomical Observatories, Chinese Academy of Sciences, Beijing 100101, China

<sup>2</sup>University of Chinese Academy of Sciences, Beijing 100049, China

<sup>3</sup>School of Physics and Electronics, Qiannan Normal University for Nationalities, Duyun 558000, China

<sup>4</sup>RAL Space, United Kingdom Research and Innovation, Science and Technology Facilities Council, Rutherford Appleton Laboratory, Harwell Campus, Oxfordshire OX11 0QX, UK

Accepted 2021 April 20. Received 2021 April 19; in original form 2020 October 1

## ABSTRACT

Observations of interplanetary scintillation (IPS) are an efficient remote-sensing method to study the solar wind and inner heliosphere. From 2016 to 2018, some distinctive observations of IPS sources like 3C 286 and 3C 279 were accomplished with the Five-hundred-meter Aperture Spherical radio Telescope (FAST), the largest single-dish telescope in the world. Due to the 270–1620 MHz wide frequency coverage of the ultra-wideband (UWB) receiver, one can use both single-frequency and dual-frequency analyses to determine the projected velocity of the solar wind. Moreover, based on the extraordinary sensitivity owing to the large collecting surface area of FAST, we can observe weak IPS signals. With the advantages of both the wider frequency coverage and high sensitivity, and also with our radio frequency interference (RFI) mitigation strategy and an optimized model-fitting method, in this paper we analyse the fitting confidence intervals of the solar wind velocity and present some preliminary results achieved using FAST, which point to the current FAST system being highly capable of carrying out observations of IPS.

**Key words:** scattering – methods: data analysis – sun: heliosphere – solar wind.

## 1 INTRODUCTION

While coming through the solar wind plasma, the radio signal from a distant compact radio source is scattered by the density inhomogeneities of the solar wind; consequently a random diffraction pattern is observed on Earth. This phenomenon is known as interplanetary scintillation (IPS) (Hewish, Scott & Wills 1964). In turn, these ground-based IPS observations can be used to infer the physical properties of the solar wind. Nowadays, as space exploration and technologies are growing, solar-activity monitoring and space-weather forecasting are becoming more critical. Although the solar wind can be observed directly using an *in situ* satellite/spacecraft with relatively high accuracy, ground-based observations of IPS provide a more economical method to obtain information on the solar wind such as velocity, as well as the structure of a sub-arcsecond-scale compact radio source (Hewish & Symonds 1969; Armstrong & Coles 1972). Another advantage of IPS observations is that the solar wind can be monitored with a longer time-scale and a more flexible spatial range out of the ecliptic plane. Besides solar physics, IPS observations can also be used to study space weather.

Since the IPS phenomenon was discovered in the 1960s (Clarke 1964; Hewish et al. 1964), many countries, including the UK, USA, Japan, India, and Russia, have undertaken IPS studies. Some astronomical instruments were built exclusively for IPS observations,

like the multistation system in Japan (Asai et al. 1995). Another successful example is called the Ooty Radio Telescope (ORT), located in India (Manoharan & Ananthkrishnan 1990). These two facilities are both based on a parabolic cylinder design using a central observing frequency of 327 MHz. Since observations of IPS are an effective way to study heliospheric physics, some new facilities for IPS studies have been built or are going to be built, like the Mexican Array Radio Telescope (MEXART) (Mejia-Ambriz et al. 2010; Chang, Gonzalez-Esparza & Mejia-Ambriz 2016) in Mexico, and a new IPS telescope system to be constructed in Inner Mongolia, China, which is an array with three 140 × 40 m cylinder antennas at Mingantu, together with two 16 m parabolic antennas at Abaga and Keshiketeng (Yan et al. 2018). Furthermore, other radio telescopes, like the Murchison Widefield Array (MWA) (Kaplan et al. 2015), Low Frequency Array (LOFAR) (Fallows et al. 2013), and Square Kilometre Array (SKA) (Nakariakov et al. 2015; Nindos, Kontar & Oberoi 2019), have also adopted IPS investigations as one of their scientific goals.

Observations of IPS can be conducted either by a single station or by multistations (Armstrong & Coles 1972; Coles & Kaufman 1978; Zhang 2007; Bisi et al. 2010a,b). The four-station system in Japan is an example of a multistation system, and it can measure the radial solar wind projection (Asai et al. 1995). Due to some practical reasons, most IPS facilities have adopted the single-station system, like ORT (Manoharan 2010), MWA (Morgan et al. 2018; Chhetri et al. 2018a,b), and the 25 m radio telescope in Urumqi, Xinjiang, China (Liu et al. 2010). For single-station observations, two analysis modes are available, dependent on the system observing capabilities, namely the single-frequency (SSSF) and dual-frequency (SSDF)

\* E-mail: [pb@nao.cas.cn](mailto:pb@nao.cas.cn) (BP); [yulei@nao.cas.cn](mailto:yulei@nao.cas.cn) (LY); [bliu@nao.cas.cn](mailto:bliu@nao.cas.cn) (BL)

**Table 1.** Key observation parameters of ORT and FAST.  $T_{\text{sys}}$  for FAST is provided at 327 MHz for direct comparison with ORT.

Facility	$T_{\text{sys}}$ (K)	$A_{\text{eff}}$ ( $\text{m}^2$ )
ORT	150	8000
FAST	70	49 500

analysis modes (Zhang 2007). In the single-frequency analysis, the solar wind velocity can be calculated from a multiparameter model fitting or from the characteristic frequencies of the power spectrum. For the dual-frequency analysis, the solar wind velocity can be drawn from the first zero-crossing frequency of the normalized co-spectrum (NCS).

In China, IPS observations started in the 1990s with the Miyun Synthesis Radio Telescope (MSRT) at Miyun station, which was run by the Beijing Astronomical Observatory (BAO), Chinese Academy of Sciences, now called the National Astronomical Observatories, Chinese Academy of Sciences (NAOC) (Ma 1993; Zhang & Wu 2001; Wu, Zhang & Zheng 2001), which is an array of 28 single dishes. The effective area of MSRT is equal to a 47 m single dish, with an observing frequency of 232 MHz.

An IPS quasi-regular observation system was established with the 25 m radio telescope in Urumqi (Liu et al. 2010) in 2008, with a central observing frequency of 1.4 GHz. It is the first IPS observation system launched in a single dish in China. The observing frequencies of the telescopes in Ooty and at the Solar–Terrestrial Environment Laboratory, Nagoya University (STELab, now called ISEE) are both 327 MHz. Since IPS observations can capture distance information corresponding to frequencies, one can obtain information relatively closer to the Sun (Scott, Rickett & Armstrong 1983) while observing IPS sources at higher frequencies; therefore the Urumqi telescope can obtain information on positions approaching less than 18 solar radii (Zhang 2007).

In 2006 a mega-science project in China was launched, called the Meridian Space Weather Monitoring Project (Meridian Project for short). There is a subsystem of this project to develop ground-based IPS observations, which is configured on the 50 m telescope at Miyun station run by NAOC. There are two dual-frequency receivers available in this system; one is centred at 327/611 MHz and the other is centred at 2300/8400 MHz. The bandwidths of the four central frequencies are 40, 40, 300, and 800 MHz respectively. This IPS facility aimed to obtain the solar wind velocity and scintillation-index information for space-weather forecasting (Zhu et al. 2012). In the near future, an IPS facility will be built in Inner Mongolia for the National Meridian Project 2 (Yan et al. 2018), which is a three-station system with observing frequencies centred at 327 MHz, 654 MHz, and 1.4 GHz.

The Five-hundred-meter Aperture Spherical radio Telescope (FAST) was constructed successfully in Pingtang County, Guizhou province, China in 2016. In the commissioning phase, some preliminary IPS observations were carried out. The observation parameters of FAST and ORT (Oberoi 2000) are given in Table 1. According to Table 1, to observe a target source of 1 Jy with an integration time of 1 s with a typical bandwidth of 4 MHz, FAST can achieve a signal-to-noise ratio (S/N) of 95, while ORT reaches an S/N of 25 with the same settings. Based on the high sensitivity of FAST and the wide frequency coverage of the ultra-wideband (UWB) receiver, we can observe weak IPS phenomena within a short time and analyse the



**Figure 1.** A picture of FAST (a), equipped with the ultra-wideband (UWB) receiver (b).

confidence intervals associated with solar wind velocity, as reported in Section 3.

The IPS observation with FAST is introduced in Section 2. The data reduction is presented in Section 3. Discussions and concluding remarks are then presented in Section 4.

## 2 IPS OBSERVATION WITH FAST

Since 1993, astronomers and engineers from different countries including China have been involved in an ambitious international science project, later referred to as the Square Kilometre Array (SKA) with a collecting area of one square kilometre. The location of FAST was a potential candidate site for the SKA (Peng et al. 1997; Peng, Nan & Su 2000b) as the Chinese SKA programme (Peng & Nan 2002). FAST is now the largest single-dish radio telescope in the world (Fig. 1a), with a unique sensitivity to carry out some revolutionary scientific goals, like surveying neutral hydrogen in the universe, detecting faint and rare types of pulsars, looking for the first shining stars, etc. (Peng et al. 2000a; Nan et al. 2011).

After the first light of FAST observations in 2016 September, FAST entered into its commissioning phase. Some calibrators used in the FAST testing phases are IPS sources such as 3C 286 and 3C 279. As a result of the big collecting area, FAST has an extraordinary sensitivity, which is shown in Table 1. Compared to other telescopes, the unique high sensitivity of FAST improves the capability of weak signal detection in IPS observations. As a result, a series of IPS experiments was completed successfully by this giant radio telescope.

The aperture diameter of FAST is 500 m with frequency coverage from 70 MHz to 3 GHz. The high-frequency end will be extended to 8 GHz in future upgrades (Nan et al. 2011). From 2016 July to 2018 May, before the installation of the 19-beam receiver, the ultra-wideband (UWB) receiver (Fig. 1b) was used, with which all IPS data were observed. This receiver covers a frequency range of 270–1620 MHz.

Like other observing systems, the IPS observing system in FAST consists of the dish, UWB receiver, digital backend, and the data-processing pipeline. The UWB receiver mounted on FAST has a large bandwidth ratio of 1:6. The wide coverage feature can effectively reduce the number of receivers. The entire bandpass of the Reconfigurable Open Architecture Computing Hardware (ROACH) for data collection is divided into multibands; the data quality is flexibly controlled and can be explicitly displayed and checked. In order to obtain both on-source and off-source data, the tracking mode of FAST was used for our IPS observations.

The FAST UWB receiver has a digital acquisition backend that includes two polarizations designed for pulsar observation, which is suitable for IPS observations. The sampling interval of 0.1 ms is

**Table 2.** Details of observations.

Source	Dates (2017)	Sampling rate (ms)	Duration time (min)
3C 286	Nov 13, 17	0.1	10
3C 279	Nov 13, 18	0.1	10

sufficient for IPS studies. The data acquisition of the UWB receiver is separated equally into two bands. The low-frequency band covers 270–800 MHz and the high-frequency band covers 1200–1620 MHz. Both bands are then divided into multichannels, with each channel covering a frequency window of 0.25 MHz.

### 3 DATA REDUCTION

From late 2016 to 2018 May, a series of experimental IPS observations was carried out with FAST. After some system testing, debugging, and calibration, the IPS observation first made use of the calibration data from FAST to monitor the solar wind. The sources observed, typical sampling rates, dates, and duration times of the observations are given in Table 2.

Equipped with the wideband receiver, observations of IPS with FAST can be conducted with both the SSSF and SSDF analysis methods simultaneously, which helps us to get the solar wind velocity ( $V$ ); the anisotropic axial ratio ( $AR$ ), which is the ratio of the major to the minor axis of the density irregularity (Yamauchi et al. 1998); the spectral index of electron density fluctuation ( $\alpha$ ); and source size ( $\theta_0$ ) with high precision. During the commissioning phase, the high-frequency band system was not very stable; therefore our discussions are focused on the low-frequency band data.

In this section, the data-reduction pipeline and data-processing procedure is introduced, including the choice of IPS observing frequency, bandwidth, the length of time series, and a model-fitting method to obtain the solar wind velocity.

#### 3.1 Data-reduction pipeline

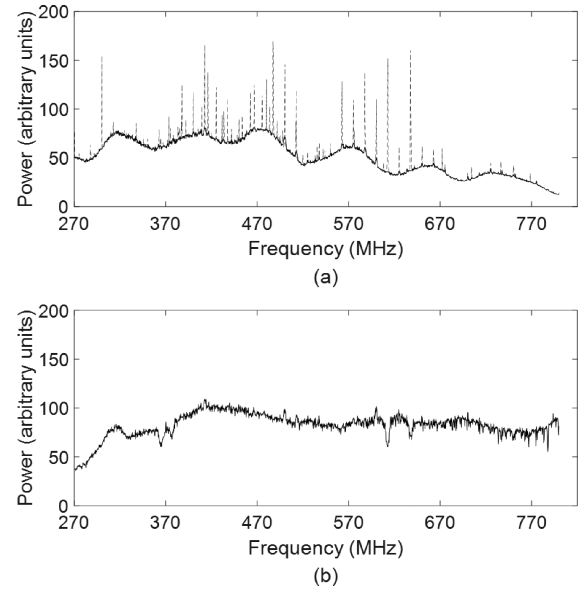
For IPS data processing, the radio frequency interference (RFI) in the data recorded by the UWB receiver is first removed, to form a new time series that is integrated both on time and frequency.

Fig. 2 demonstrates a data sample of the 270–800 MHz frequency spectrum collected by the UWB receiver with a duration time of 20 ms. The target source was 3C 286, and was observed on 2017 November 13. In Fig. 2(a) the dashed and solid lines are the frequency spectrum before and after RFI removal respectively. Fig. 2(b) is the normalized spectrum that has eliminated the systematic instrumental response between different frequencies. The broad-band fluctuation in the bandpass is probably due to standing waves, while the strong narrow-band lines are caused by RFI. It is obvious that, after removing RFI, interference throughout the whole bandpass is significantly suppressed. For traditional receivers, the acquisition data are summed throughout the whole bandwidth, which will cause some uncertainty in the collected data; therefore, it is essential to remove RFI. However, the multichannel design in the FAST UWB receiver in a radio-quiet location allows us to identify the channels with RFI and remove it more effectively.

A general expression for the telescope-observed signal is:

$$S_{\text{obs}} = S_{\text{sig}} + \varepsilon + S_{\text{RFI}}, \quad (1)$$

where  $S_{\text{obs}}$  is the observed signal,  $S_{\text{sig}}$  is the signal of interest (SOI),  $\varepsilon$  is the additive background white Gaussian noise, and  $S_{\text{RFI}}$  is



**Figure 2.** The frequency spectrum of the FAST ultra-wideband (UWB) receiver showing a standing-wave pattern. The frequency coverage of this spectrum is 270–800 MHz, with a duration of 20 ms. The target source was 3C 286, and was observed on 2017 November 13. (a) The dashed and solid lines are the frequency spectrum before and after RFI removal respectively. (b) The normalized spectrum that has eliminated the systematic instrumental response between different frequencies.

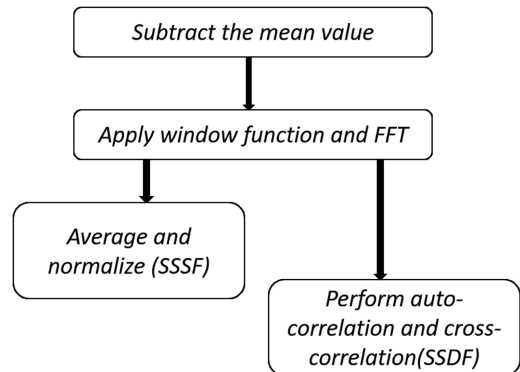


**Figure 3.** The data-reduction pipeline for SSSF and SSDF analyses.

RFI. We assume that the rms of the SOI with noise is different from RFI. Because the baseline of the frequency spectrum is very complicated, we use the rate of change of the SOI rather than the spectrum itself to identify SOI and RFI. Then a random sample consensus (RANSAC) is applied to remove RFI. The main steps are: 1) initializing the hyperparameters (inner point ratio and tolerance boundary) and fitting-model selection (a line model); 2) convolving the spectrum with the Laplacian of the Gaussian filter; 3) fitting the line model and identifying the inner and outer data; 4) doing average interpolation for the outer data; and 5) repeating steps 2–4 until convergence of the spectrum rms. The narrow-band RFI can be correctly removed by this method and, based on that, elimination of the relatively wideband RFI can be achieved iteratively.

The bandwidth of each point of these new data is 10 MHz with an integration time of 20 ms. The data-reduction pipeline (Fig. 3) is described as follows: 1) the new data set is divided into some subsets, with 512 data points and a duration time of about 10 s. Each subset

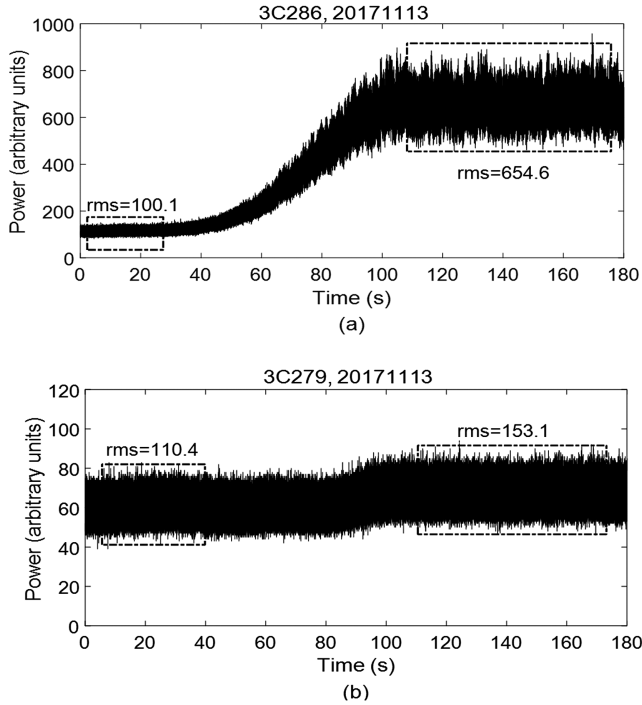


**Figure 4.** The off-(on)-source raw data of 3C 286 (a) and 3C 279 (b) observed at 305 MHz on 2017 November 13; the four rectangles represent the on-source and off-source fluctuations.

is subtracted by its average since the IPS phenomenon only relates to the flux variance; 2) we apply a fast Fourier transform (FFT) to obtain the power spectrum, from which one can extract variance information on a frequency scale. The data sample is smoothed using a Hanning window as the window function so as to reduce the cut-off effects of the FFT; and 3) we average the spectrum of two subsets and normalize it to form the SSSF power spectrum with a time duration of 20 s. There is some observational evidence for AR being close to unity when the solar elongation is larger than  $15^\circ$  (Coles & Kaufman 1978; Yamauchi et al. 1996), meaning that the low-frequency part of the SSSF power spectrum is almost flat. The elongation of 3C 286 on 2017 November 13 was beyond  $30^\circ$ . So in the rest of this paper, the data points of 3C 286 below 0.7 Hz are set to be the same value. Data-processing steps 1–3 are subsequently applied to the SSSF analysis. The last step is the SSDF analysis based on Scott et al. (1983), which takes the FFT outputs from step 2 to perform auto-correlation and cross-correlation for each dual-frequency pair.

### 3.2 Data-processing results

The IPS observation was intended to monitor the solar wind and to calculate the velocity and scintillation index. The UWB receiver is capable of taking data over very wide bandwidths that can be split up and analysed very flexibly, thus making it possible to perform both SSSF and SSDF analyses on the same data set simultaneously. Furthermore, any observing frequency bands could be chosen flexibly. Since there was no extra observation time to be applied, calibrators like 3C 286 and 3C 279 are chosen for our IPS study.

The on- and off-source raw data of 3C 286 and 3C 279 observed on 2017 November 13 are shown in Figs 4(a) and (b) respectively. The observing frequency is centred at 305 MHz. The fluctuation levels

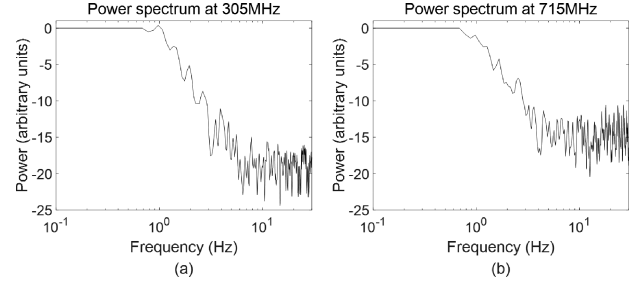


**Figure 5.** SSSF-analysis-mode power spectra for 3C 286 at 305 MHz (a) and 715 MHz (b) on 2017 November 13.

for on- and off-source observations have a significant difference, as shown in Figs 4(a) and (b). There is obvious discrimination as shown in the two rectangles in Fig. 4(a), while in Fig. 4(b) the fluctuations in the two rectangles are at a similar level. This is also reflected in the rms values. So the scintillation level of 3C 286 that day was stronger than that of 3C 279. In the following, the results derived from the observation on 3C 286 are discussed as an example.

Fig. 5 demonstrates the SSSF-analysis-mode power spectrum of the source 3C 286 observed on 2017 November 13. The central frequencies for Figs 5(a) and (b) are 305 and 715 MHz, respectively, each of which has a bandwidth of 10 MHz. Fig. 5 clearly shows that the power spectrum at 305 MHz has a higher scintillation level than the spectrum at 715 MHz. According to equation (2), the scintillation index  $m$  (Cohen et al. 1967) is 0.09 for the low frequency and 0.08 for the high frequency, where  $C_{\text{on}}$  ( $C_{\text{off}}$ ) is the average intensity of the on-source (off-source) signal and  $\sigma_{\text{on}}^2$  ( $\sigma_{\text{off}}^2$ ) is the square of the rms of intensity scintillation:

$$m = \frac{\sqrt{\sigma_{\text{on}}^2 - \sigma_{\text{off}}^2}}{C_{\text{on}} - C_{\text{off}}}. \quad (2)$$

### 3.3 Model fitting

The solar wind velocity from SSSF analysis can be obtained either by 1) a characteristic frequency called the Fresnel knee frequency; or 2) by model fitting via some parameters. In equation (3) (Scott et al. 1983),  $V$  stands for the solar wind velocity,  $f_F$  the Fresnel knee frequency,  $z$  the distance to the scattering screen, and  $\lambda$  the wavelength of the observing frequency:

$$V = f_F \sqrt{z \lambda \pi}. \quad (3)$$

In the case in which the model-fitting theoretical model used for SSSF analysis is given for the weak scintillation region, the formula can be represented by a theoretical temporal power spectrum  $P(f)$ , which is shown in equation (4), where  $f$  is the temporal frequency,  $C = (2\pi r_e \lambda)^2$  is a constant related to the observing wavelength  $\lambda$ , and  $r_e$  is the electron radius:

$$P(f) = C \int_{-z}^z \frac{1}{V(z)} dz \int_{-\infty}^{+\infty} \Phi_{ne} F_{\text{diff}} F_{\text{source}} dq_y. \quad (4)$$

In equation (4), the spectrum of the electron-density fluctuations  $\Phi_{ne} \propto q^{-\alpha}$ , where  $q = \sqrt{q_x^2 + q_y^2 + q_z^2}$  is the three-dimensional wavenumber.  $F_{\text{diff}}$  is the Fresnel propagation filter and  $F_{\text{source}}$  is the squared modulus of the source visibility (Manoharan & Ananthakrishnan 1990; Mejia-Ambriz et al. 2015; Chang et al. 2019).

In some previous studies, the fitting parameters like AR and  $\alpha$  are often set to be a fixed number for simplicity, and the model fitting (Oberoi 2000) is done just by adjusting the solar wind velocity  $V$ . In

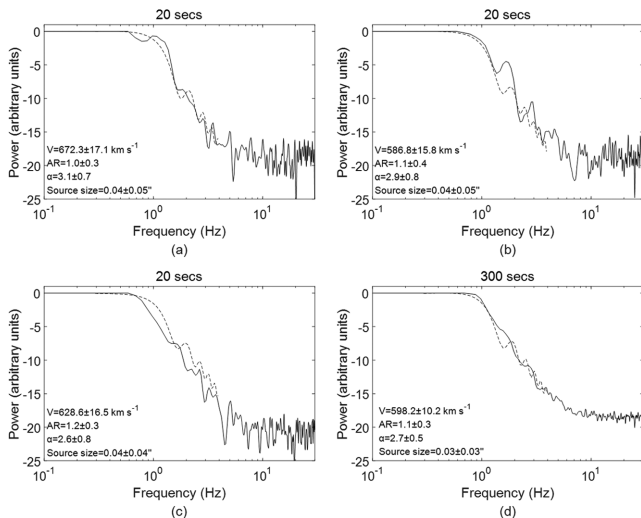


**Figure 6.** The model-fitting example of source 3C 286 with SSSF analysis mode; the central observing frequency is 285 MHz. The solid and dashed lines show the observed and fitting spectra respectively. (a)–(c) show the results for the time length of 20 s, and (d) shows that of 300 s.

our IPS studies, a numerical optimization applies a weighted trust-region reflective least-squares (TRRLS) algorithm to optimize the four parameters (including  $V$ ,  $AR$ ,  $\alpha$ , and source size of the radio source) of the IPS model, which are based on physical constraints. The fitting parameters are obtained by fitting the theoretical model to the actual power spectrum. We used the 95 per cent confidence intervals as the error bars of the parameters. Moreover, the multi-initialization strategy applied will guarantee the fitting convergence in the global minimization. In order to obtain good performance in the fitted velocity, we used the weighted non-linear least-squares fitting. The objective function of this method is:

$$\min \frac{1}{N_m} \sum_{i=1}^{N_m} W(i) \|\lg(P_m(V, AR, \alpha, \theta_0)) - \lg(P_{\text{obs}})\|_2^2, \quad (5)$$

where  $N_m$  is the number of points that will be used to carry out model fitting,  $W$  is weight, and  $P_m(V, AR, \alpha, \theta_0)$  and  $P_{\text{obs}}$  are the IPS model and observed power spectra, respectively.

Fig. 6 shows some examples of the SSSF model-fitting results of 3C 286 with different time lengths; the central observing frequency is set to be 285 MHz. The solid and dashed lines show the observed and model-fitting spectra respectively. The time length of the power spectra of Figs 6(a)–(c) is 20 s, and that of Fig. 6(d) is 300 s. Table 3 gives the parameters with error bars obtained by a data set of 300 s; each velocity is obtained with a 20 s time length. The corresponding value for data with 300 s are:  $V = 598.2 \pm 10.2 \text{ km s}^{-1}$ ,  $AR = 1.1 \pm 0.3$ ,  $\alpha = 2.7 \pm 0.5$ , source size =  $0.03 \pm 0.03''$ . The weighted mean values with scatter for each column of Table 3 are:  $V = 620.9 \pm 4.1 \text{ km s}^{-1}$ ,  $AR = 1.1 \pm 0.1$ ,  $\alpha = 2.8 \pm 0.2$ , and source size =  $0.04 \pm 0.01''$ . According to ISEE, the solar wind velocity obtained from observations of 3C 286 on 2017 November 14 was  $609 \text{ km s}^{-1}$ . It can be concluded that the resulting solar wind velocity with the data of 20 s integration is consistent with the ones with the time length of 300 s. That means that the model-fitting method developed is applicable; therefore, with the high sensitivity of FAST, the solar wind velocity can be derived from a 20 s observation for this source that day.

**Table 3.** Fitted parameters with error bars for the 300 s observation divided up into 20 s intervals using the SSSF analysis method on the central frequency of 285 MHz with a 10 MHz bandwidth. We used the 95% confidence intervals as the error bars of the parameters. The last row demonstrates the weighted mean values with scatter for each column.

$V$ ( $\text{km s}^{-1}$ )	$AR$	$\alpha$	Source size (arcsec)
626.2 ± 14.5	1.1 ± 0.4	2.7 ± 0.7	0.04 ± 0.04
636.4 ± 17.5	1.1 ± 0.3	2.8 ± 0.8	0.04 ± 0.05
552.4 ± 11.4	1.1 ± 0.2	3.0 ± 0.5	0.01 ± 0.09
672.3 ± 17.1	1.0 ± 0.3	3.1 ± 0.7	0.04 ± 0.05
623.3 ± 20.6	1.1 ± 0.4	2.9 ± 0.7	0.01 ± 0.12
663.4 ± 18.2	1.0 ± 0.3	3.3 ± 0.8	0.01 ± 0.19
586.8 ± 15.8	1.1 ± 0.4	2.9 ± 0.8	0.04 ± 0.05
749.1 ± 17.1	1.0 ± 0.3	3.1 ± 0.7	0.04 ± 0.05
577.2 ± 20.6	1.0 ± 1.0	1.6 ± 0.9	0.04 ± 0.05
628.6 ± 16.5	1.2 ± 0.3	2.6 ± 0.7	0.04 ± 0.04
624.7 ± 14.7	1.0 ± 0.4	2.7 ± 0.6	0.04 ± 0.04
647.6 ± 13.1	1.0 ± 0.3	3.3 ± 0.5	0.01 ± 0.14
579.5 ± 11.9	1.0 ± 0.4	2.5 ± 0.5	0.04 ± 0.03
560.7 ± 14.6	1.1 ± 0.5	2.4 ± 0.7	0.04 ± 0.04
642.3 ± 22.9	0.9 ± 0.7	1.8 ± 1.2	0.07 ± 0.05
620.9 ± 4.1	1.1 ± 0.1	2.8 ± 0.2	0.04 ± 0.01

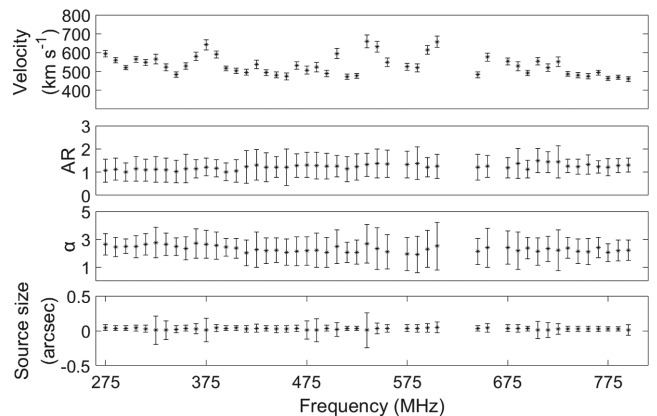


**Figure 7.** The solar wind parameters from the 10 MHz bandwidth subbands using the 20 s time length. The four parameters, velocity,  $AR$ ,  $\alpha$ , and source size, are shown from top to bottom. The subbands affected by strong RFI are rejected. The stars and solid lines represent the fitting values and the error bars.

The low-frequency band of the FAST UWB receiver covers a wide frequency range from 270–800 MHz, which is divided into 53 subbands, and each subband covers a frequency bandwidth of 10 MHz. Fig. 7 shows the results of the four fitting parameters ( $V$ ,  $AR$ ,  $\alpha$ , and source size) obtained from each subband; the bands affected by strong RFI are rejected. The time length for each result is 20 s. The stars and solid lines are the fitting values and the error bars respectively.

The mean velocity in Fig. 7 is  $531.9 \text{ km s}^{-1}$  with a standard deviation of  $52.7 \text{ km s}^{-1}$ , revealing velocity estimates from about  $600 \text{ km s}^{-1}$  at lower frequency to  $\sim 450 \text{ km s}^{-1}$  at higher frequency, with a fractional variability of  $\sim 9.9$  per cent over a frequency range of  $\sim 500$  MHz, mostly in a linear trend. The model-fitting values of  $AR$ ,  $\alpha$ , and the source-size component tend towards constants, which also confirms why some former studies set these three parameters to

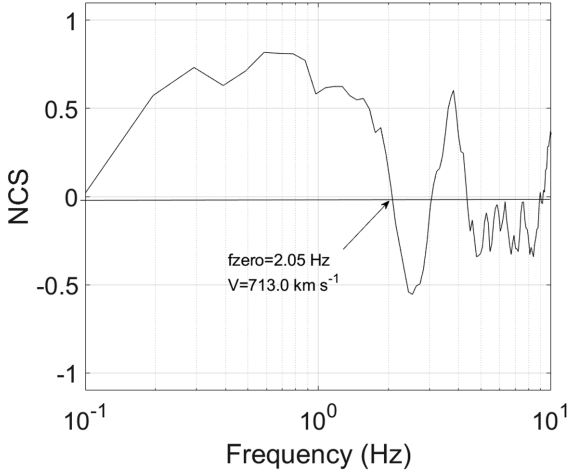


**Figure 8.** The power spectra of source 3C 286 in SSDF analysis mode, observed on 2017 November 13. The two frequencies adopted here are 305 and 715 MHz. The time length of this data set is 20 s, and the arrow shows  $f_{\text{zero}}$ .

**Table 4.** SSSF and SSDF analysis mode velocity results with a duration time of 300 s. Columns 1–3 are the frequency, velocity, and error, respectively.

Frequency (MHz)	Velocity ( $\text{km s}^{-1}$ )	Error ( $\text{km s}^{-1}$ )
305	593.4	10.2
715	465.0	7.3
305/715	747.8	–

be fixed numbers (e.g. Oberoi 2000). This means that the parameters obtained from the model-fitting methods are reliable, and the new telescope, FAST, has great advantages for investigating the inner heliosphere with IPS using both analysis types.

For SSDF analysis mode, the solar wind velocity is deduced from the first zero-crossing frequency of the NCS. In equation (6)  $\lambda_1$  is the wavelength of the lower observing frequency,  $z$  is the effective screen distance,  $f_{\text{zero}}$  is the first zero-crossing frequency of NCS, and  $A$  is a correcting factor that varies slightly with the solar wind parameters and is always set to a constant, 1 (Scott et al. 1983; Tokumaru et al. 1994; Zhang 2007):

$$V = A f_{\text{zero}} \sqrt{z \lambda_1}. \quad (6)$$

Fig. 8 shows the result of the SSDF spectrum of 3C 286 observed on 2017 November 13. The two observing frequencies are 305 MHz and 715 MHz. The time length of the data set is 20 s, the arrow shows the first crossing frequency  $f_{\text{zero}}$  of the NCS, which is 2.05 Hz, and the deduced solar wind velocity is  $713.0 \text{ km s}^{-1}$ . The velocities at the same time length from the SSSF analysis mode are  $564.4 \pm 16.5 \text{ km s}^{-1}$  (305 MHz) and  $554.2 \pm 19.6 \text{ km s}^{-1}$  (715 MHz) taken from Fig. 7, which are consistent with the velocity variation trend observed in Fig. 7. Table 4 presents the velocity results of the SSSF and SSDF analysis modes with a duration time of 300 s. Columns 1–3 show the frequency, velocity, and error, respectively. It can be seen that the velocities deduced from 20 s are consistent with the results of 300 s. The velocity deduced from SSDF analysis mode is likely to be affected by the random velocity (Tokumaru et al. 1994); this may be why the velocity of SSDF is higher than the velocity obtained from SSSF analysis mode, or it may be that the IPS is weak at that time, so the reliability of the velocity determination

**Table 5.** The effect of different  $\Delta f$ . Columns 1–5 show  $f_1$ ,  $f_2$ ,  $\Delta f$ ,  $f_{\text{zero}}$ , and  $V$  respectively.

$f_1$ (MHz)	$f_2$ (MHz)	$\Delta f = f_2 - f_1$ (MHz)	$f_{\text{zero}}$ (Hz)	$V$ ( $\text{km s}^{-1}$ )
285	335	50	3.516	1265.1
285	385	100	2.148	772.9
285	435	150	2.051	737.9
285	485	200	2.051	737.9
285	535	250	2.051	737.9
285	585	300	2.051	737.9
285	635	350	2.051	737.9
285	685	400	2.148	772.9
285	735	450	2.051	737.9
285	785	500	2.051	737.9

is reduced. In any case, the cause of the difference in velocity still needs further study.

#### 4 DISCUSSIONS AND CONCLUDING REMARKS

There are four remarkable advantages to carrying out IPS observations with the newly established telescope, FAST. First, FAST is incredibly sensitive in searching for weak signals owing to its uniquely large collecting area, which allows us to obtain solar wind velocity information in a short observation of  $\sim 20$  s. Since the IPS is a fast-changing phenomenon with a time-scale of  $\sim 1$  s (Cohen 1969), the long integration is likely to obscure the scintillation phenomena. Secondly, the bandwidth can be chosen flexibly. Otherwise, if the adopted bandwidth is larger than the coherence scales, the scintillation will be smeared because the IPS is a frequency-dependent phenomenon (Little 1968). Thirdly, with the wide frequency coverage of the receiver and multichannels, IPS observations in SSSF and SSDF analysis modes can be conducted with FAST simultaneously. The velocities derived from the two analysis modes provide a good supplement. In addition, IPS studies do not require a great deal of extra and dedicated observing time, for if the position of the source is appropriate we can take most calibrators as IPS targets that can accommodate a symbiotic project.

Because of the wide frequency coverage of the UWB receiver, we can also study the effect of different frequency differences in the SSDF analysis mode. Table 5 shows the result of a comparison of different frequency differences  $\Delta f$  ( $\Delta f = f_2 - f_1$ ).  $f_1$  in Table 5 is set to be 285 MHz. The five columns are two observing frequencies,  $\Delta f$ , the first zero-crossing frequency, and the deduced solar wind velocity. It can be concluded from Table 5 that, when  $\Delta f$  is bigger than 30 per cent of  $f_1$ , then the deduced  $f_{\text{zero}}$  tends to be stable. The reason for these frequency differences still requires some follow-up study.

Our preliminary results demonstrate that FAST has outstanding potential to perform observations of IPS. By comparing the solar wind velocities calculated from the SSDF and SSSF analysis modes, the reliability of observation is proved. In general, taking advantage of the high sensitivity and wide frequency coverage as well as the multichannel design of the UWB receiver, the observation time with FAST can significantly decrease for each IPS source, and the choice of frequencies is flexible to get rid of RFI-contaminated data.

We conclude that a larger number of target sources can be observed with FAST on a short time-scale. Therefore, IPS data from FAST will widen the range of observable solar–terrestrial space and improve the accuracy of solar wind velocity estimates. This can be further utilized in space-weather forecasts.

## ACKNOWLEDGEMENTS

This work is supported by the National Key R&D Programme of China under grant number 2018YFA0404703, the Open Project Programme of the CAS Key Laboratory of FAST, NAOC, Chinese Academy of Sciences, and the basic research programme and project of Yunnan province, China (2019FB009). The authors thank all the staff of JLRAT, NAOC, for their help during the observations. We are grateful to Yu-Hai Qiu, Xi-Zhen Zhang, Cheng-Min Zhang, Ming Xiong (National Space Science Center, CAS), R. A. Fallow (ASTRON), M. Tokumaru (Solar–Terrestrial Environment Laboratory, Nagoya University, Nagoya, Japan), and Julio Mejia-Ambriz (SCiESMEX, Instituto de Geofísica, Unidad Michoacán, Universidad Nacional Autónoma de México) for their helpful discussions. The authors also thank Yue Ma and Sivasankaran Srikanth (National Radio Astronomy Observatory, NRAO) for their help in polishing the English. OC acknowledges the European Union Horizon 2020 research and innovation programme under the Marie Skłodowska-Curie grant agreement 665593 awarded to the Science and Technology Facilities Council. MMB acknowledges STFC in-house research funding to RAL Space under the STFC Astronomy Grants Panel Consolidated Grants Programme. This work has made use of data from FAST (Five-hundred-meter Aperture Spherical radio Telescope). FAST is a Chinese national mega-science facility, operated by the National Astronomical Observatories, Chinese Academy of Sciences.

## DATA AVAILABILITY

The raw data underlying this article cannot be shared publicly due to the data policy of FAST. The intermediate-process data will be shared on reasonable request to the corresponding author.

## REFERENCES

Armstrong J. W., Coles W. A., 1972, *J. Geophysical Res.*, 77, 4602  
 Asai K., Ishida Y., Kojima M., Maruyama K., Misawa H., Yoshimi N., 1995, *J. Geomagnetism Geoelectricity*, 47, 1107  
 Bisi M. M., Fallows R. A., Breen A. R., O’Neill I. J., 2010a, *Sol. Phys.*, 261, 149  
 Bisi M. M. et al., 2010b, *Sol. Phys.*, 265, 49  
 Chang O., Gonzalez-Esparza J. A., Mejia-Ambriz J., 2016, *Advances Space Res.*, 57, 1307  
 Chang O., Bisi M. M., Aguilar-Rodriguez E., Fallows R. A., Gonzalez-Esparza J. A., Chashei I., Tyul’bashev S., 2019, *Space Weather*, 17, 1114  
 Chhetri R., Morgan J., Ekers R. D., Macquart J. P., Sadler E. M., Giroletti M., Callingham J. R., Tingay S. J., 2018a, *MNRAS*, 474, 4937  
 Chhetri R., Ekers R. D., Morgan J., Macquart J. P., Franzen T. M. O., 2018b, *MNRAS*, 479, 2318  
 Clarke M. E., 1964, PhD thesis, Cambridge Univ.  
 Cohen M. H., 1969, *ARA&A*, 7, 619  
 Cohen M., Gundermann E., Hardebeck H., Sharp L., 1967, *ApJ*, 147, 449

Coles W., Kaufman J., 1978, *Radio Sci.*, 13, 591  
 Fallows R. A., Asgekar A., Bisi M. M., Breen A. R., ter-Veen S., 2013, *Sol. Phys.*, 285, 127  
 Hewish A., Symonds M., 1969, *Planet. Space Sci.*, 17, 313  
 Hewish A., Scott P., Wills D., 1964, *Nature*, 203, 1214  
 Kaplan D. L. et al., 2015, *ApJ*, 809, L12  
 Little L., 1968, *Planet. Space Sci.*, 16, 749  
 Liu L.-J., Zhang X.-Z., Li J.-B., Manoharan P., Liu Z.-Y., Peng B., 2010, *Res. Astron. Astrophys.*, 10, 577  
 Ma G. Y., 1993, PhD thesis, Beijing Astronomical Observatory, Chinese Academy of Sciences  
 Manoharan P. K., 2010, *Sol. Phys.*, 265, 137  
 Manoharan P., Ananthakrishnan S., 1990, *MNRAS*, 244, 691  
 Mejia-Ambriz J. C., Villanueva-Hernandez P., Gonzalez-Esparza J. A., Aguilar-Rodriguez E., Jeyakumar S., 2010, *Sol. Phys.*, 265, 309  
 Mejia-Ambriz J. C., Jackson B. V., Gonzalez-Esparza J. A., Buffington A., Tokumaru M., Aguilar-Rodriguez E., 2015, *Sol. Phys.*, 290, 2539  
 Morgan J. S. et al., 2018, *MNRAS*, 473, 2965  
 Nakariakov V. et al., 2015, Proc. Advancing Astrophysics with the Square Kilometre Array (AASKA14). Giardini Naxos, Italy, p. 169  
 Nan R. et al., 2011, *Int. J. Modern Phys. D*, 20, 989  
 Nindos A., Kontar E. P., Oberoi D., 2019, *Advances Space Res.*, 63, 1404  
 Oberoi D., 2000, PhD thesis, Department of Physics, Indian Institute of Science  
 Peng B., Nan R., 2002, *Radio Sci. Bull.*, 300, 12  
 Peng B., Nan R., Qiu Y., Nie Y., Zhu B., Xu X., Strom R., 1997, Further Site Survey for the Next-Generation Large Radio Telescope in Guizhou. Cambridge University Press, Cambridge, UK, p. 278  
 Peng B., Strom R. G., Nan R., Ma E., Ping J., Zhu L., Zhu W., 2000a, in van Haarlem M. P., ed., Perspectives on Radio Astronomy: Science with Large Antenna Arrays. ASTRON, Netherlands, p. 25  
 Peng B., Nan R., Su Y., 2000b, in Butcher H. R., ed., Proc. SPIE Conf. Ser. Vol. 4015, Radio Telescopes. SPIE, Bellingham, p. 45  
 Scott S. L., Rickett B. J., Armstrong J. W., 1983, *A&A*, 123, 191  
 Tokumaru M., Kondo T., Mori H., Tanaka T., 1994, *J. Geomagnetism Geoelectricity*, 46, 835  
 Wu J., Zhang X., Zheng Y., 2001, *Ap&SS*, 278, 189  
 Yamauchi Y. et al., 1996, in Winterhalter D., Gosling J. T., Habbal S. R., Kurth W. S., Neugebauer M., eds, AIP Conference Proceedings. Vol. 382. Am. Inst. Phys., New York, p. 366  
 Yamauchi Y., Tokumaru M., Kojima M., Manoharan P. K., Esser R., 1998, *J. Geophysical Res.*, 103, 6571  
 Yan Y., Wang W., Chen L., Liu F., Geng L., Chen Z., 2018, *Sun and Geosphere*, 13, 153  
 Zhang X.-Z., 2007, *Chinese J. Astron. Astrophys.*, 7, 712  
 Zhang X. Z., Wu J. H., 2001, in Brekke P., Fleck B., Gurman J. B., eds, Proc. IAU Symp. 203, Recent Insights into the Physics of the Sun and Heliosphere: Highlights from SOHO and other Space Missions. Astronomical Society of the Pacific, San Francisco, p. 580  
 Zhu X.-Y., Zhang X.-Z., Zhang H.-B., Kong D.-Q., Qu H.-P., 2012, *Res. Astron. Astrophys.*, 12, 857

This paper has been typeset from a  $\text{\TeX}/\text{\LaTeX}$  file prepared by the author.